

Giant X-Ray Circular Dichroism in a Time-Reversal Invariant Antiferromagnet

Jun Okamoto, Ru-Pan Wang, Yen-Yi Chu, Hung-Wei Shiu, Amol Singh, Hsiao-Yu Huang, Chung-Yu Mou, Sukhito Teh, Horng-Tay Jeng, Kai Du, Xianghan Xu, Sang-Wook Cheong, Chao-Hung Du, Chien-Te Chen, Atsushi Fujimori,* and Di-Jing Huang*

X-ray circular dichroism, arising from the contrast in X-ray absorption between opposite photon helicities, serves as a spectroscopic tool to measure the magnetization of ferromagnetic materials and identify the handedness of chiral crystals. Antiferromagnets with crystallographic chirality typically lack X-ray magnetic circular dichroism because of time-reversal symmetry, yet exhibit weak X-ray natural circular dichroism. Here, the observation of giant natural circular dichroism in the Ni L_3 -edge X-ray absorption of Ni_3TeO_6 is reported, a polar and chiral antiferromagnet with effective time-reversal symmetry. To unravel this intriguing phenomenon, a phenomenological model is proposed that classifies the movement of photons in a chiral crystal within the same symmetry class as that of a magnetic field. The coupling of X-ray polarization with the induced magnetization yields giant X-ray natural circular dichroism, revealing typical ferromagnetic behaviors allowed by the symmetry in an antiferromagnet, i.e., the altermagnetism of Ni_3TeO_6 . The findings provide evidence for the interplay between magnetism and crystal chirality in natural optical activity. Additionally, the first example of a new class of magnetic materials exhibiting circular dichroism is established with time-reversal symmetry.

1. Introduction

The interaction of light with matter provides a powerful technique to investigate the breaking of space-inversion and time-reversal (\mathcal{T}) symmetries. One can observe circular dichroism, i.e., the differential absorption of right- and left-handed circularly polarized (RCP and LCP) light, in a crystal lacking inversion symmetry. The optical activity that measures X-ray circular dichroism (XCD) in a material with \mathcal{T} symmetry is termed X-ray *natural* circular dichroism (XNCD),^[1–3] conventionally understood to arise from the interference between electric-dipole (E1) and electric-quadrupole (E2) transitions.^[4] Natural optical activity is a reciprocal effect, as the absorption of photons moving in one direction is the same as that in the opposite direction.

For a material with broken \mathcal{T} symmetry such as a ferromagnet or a ferrimagnet,^[5,6] magnetic circular dichroism in X-ray

J. Okamoto, Y.-Y. Chu, H.-W. Shiu, A. Singh, H.-Y. Huang, C.-T. Chen, A. Fujimori, D.-J. Huang
 National Synchrotron Radiation Research Center
 Hsinchu 30076, Taiwan
 E-mail: fujimori@phys.s.u.tokyo.ac.jp; djhuang@nsrrc.org.tw

R.-P. Wang
 Department of Physics
 University of Hamburg
 Luruper Chaussee 149, G610, 22761 Hamburg, Germany

C.-Y. Mou, A. Fujimori
 Center for Quantum Science and Technology and Department of Physics
 National Tsing Hua University
 Hsinchu 30013, Taiwan

S. Teh, H.-T. Jeng, D.-J. Huang
 Department of Physics
 National Tsing Hua University
 Hsinchu 30013, Taiwan

 The ORCID identification number(s) for the author(s) of this article can be found under <https://doi.org/10.1002/adma.202309172>

© 2024 National Synchrotron Radiation Research Center (NSRRC). Advanced Materials published by Wiley-VCH GmbH. This is an open access article under the terms of the [Creative Commons Attribution-NonCommercial](https://creativecommons.org/licenses/by-nc/4.0/) License, which permits use, distribution and reproduction in any medium, provided the original work is properly cited and is not used for commercial purposes.

DOI: 10.1002/adma.202309172

K. Du, X. Xu, S.-W. Cheong
 Rutgers Center for Emergent Materials and Department of Physics and Astronomy
 Rutgers University
 Piscataway, NJ 08854, USA

C.-H. Du
 Department of Physics
 Tamkang University
 Tamsui 251, Taiwan

A. Fujimori
 Department of Physics
 University of Tokyo
 Bunkyo-Ku, Tokyo 113-0033, Japan

D.-J. Huang
 Department of Electrophysics
 National Yang Ming Chiao Tung University
 Hsinchu 30093, Taiwan

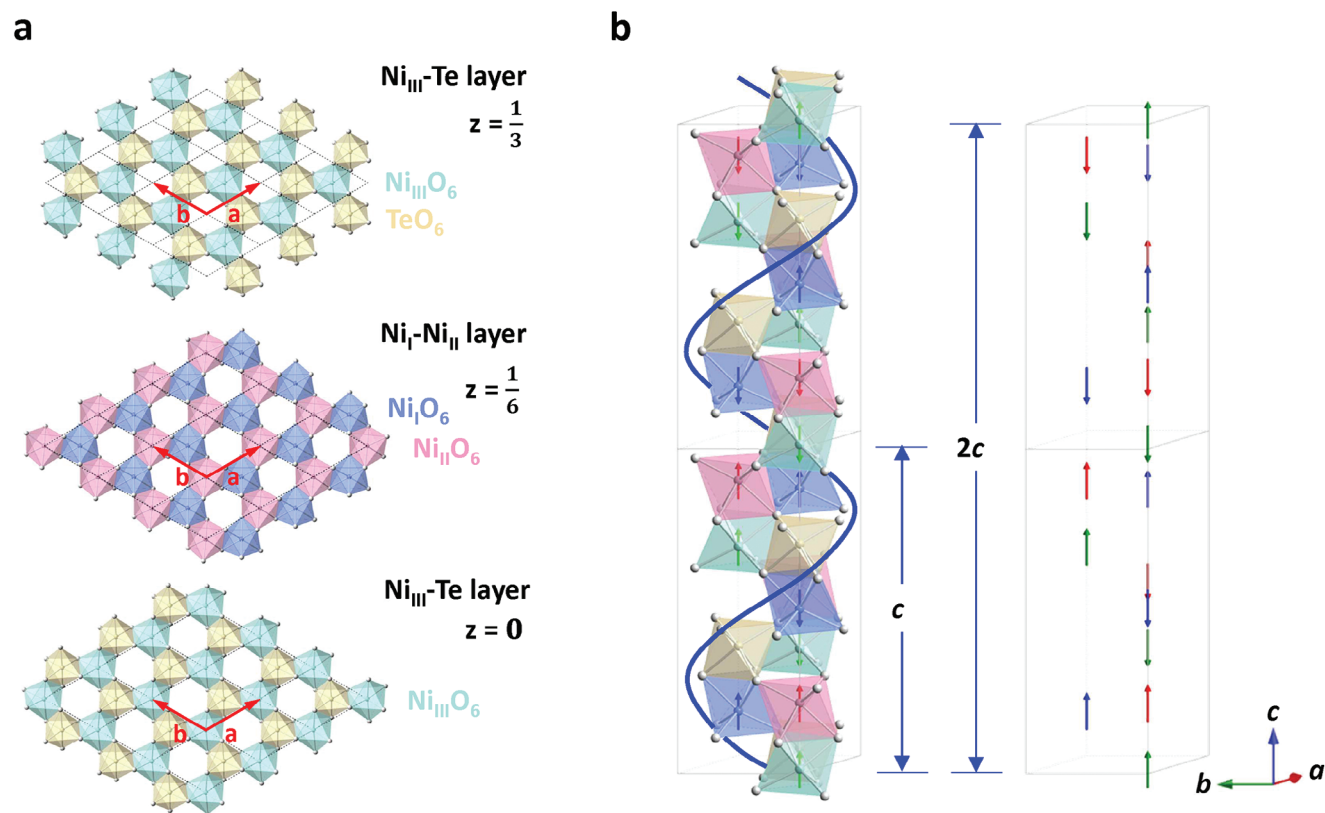


Figure 1. Crystal and spin structures of Ni_3TeO_6 . a) Two kinds of honeycomb layers in the ab plane of Ni_3TeO_6 . The $\text{Ni}_{\text{III}}\text{-Te}$ layer consists of $\text{Ni}_{\text{III}}\text{O}_6$ and TeO_6 octahedra to form a triangular lattice through edge-sharing; the $\text{Ni}_I\text{-Ni}_{\text{II}}$ layer comprises Ni_IO_6 and $\text{Ni}_{\text{II}}\text{O}_6$ octahedra. \mathbf{a} and \mathbf{b} are in-plane unit-cell vectors. The alternative stacking of the $\text{Ni}_I\text{-Ni}_{\text{II}}$ and $\text{Ni}_{\text{III}}\text{-Te}$ layers along the c axis forms the 3D rhombohedral crystal structure. The structural unit cell comprises six honeycomb layers stacked along the c axis. b) Chiral crystal structure of Ni_3TeO_6 . The blue helix represents the handedness of the crystal chirality. The spins represented by arrows are aligned along the c axis, showing the collinear antiferromagnetic structure of Ni_3TeO_6 .^[33] The magnetic unit cell consists of two structural unit cells, that is, 12 honeycomb layers stacking along the c direction. The structural unit-cell length c and the magnetic unit-cell length $2c$ are indicated by double-headed arrows.

absorption (XMCD) occurs,^[7–14] enabling the direct detection of the spin and orbital moments of an ion. While conventional understanding expects vanishing XMCD from antiferromagnetic (AFM) materials, which have no net spin moments, recent results show that XMCD can exist in AFM materials with non-collinear, namely, noncoplanar, or chiral spin structures,^[15–21] corroborating the prediction based on symmetry analysis with magnetization in relation to broken symmetries.^[22] Recently, a class of “altermagnetic” materials,^[23–26] where collinear AFM spins are fully canceled leaving no net spin moments, were found to exhibit strong XMCD due to broken \mathcal{T} symmetry.^[27]

A chiral crystal is non-superimposable on its mirror image and has well-defined handedness. Crystal chirality alone can lead to XNCD unrelated to magnetism;^[1,28] however, its magnitude is a few orders of magnitude smaller than the typical XMCD at the $L_{2,3}$ edges of $3d$ transition-metal elements. Recently, a novel kind of spontaneous Hall effect has been reported in collinear antiferromagnets with local crystal chirality.^[29] In addition, chiral crystals^[30] as well as chiral molecules including DNA on metal surfaces^[31,32] produce strong spontaneous spin polarization in charge current, referred to as chirality-induced spin selectivity (CISS).

The present Article presents the observation of the significant enhancement of XNCD by collinear antiferromagnetism. We discovered a new type of surprisingly strong XNCD at the Ni L_3 edge of the multiferroic antiferromagnet Ni_3TeO_6 , whose crystal structure is polar and chiral but the magnetic structure is collinear.^[33] Without an external magnetic field, results of X-ray absorption spectroscopy (XAS) showed that XCD changed its sign between domains of opposite crystal chirality. We explain this surprising observation through a new concept involving symmetry analysis^[34] for the mechanism of XNCD.

2. Results

2.1. Magnetic Transition of Ni_3TeO_6

Nickel tellurite Ni_3TeO_6 crystallizes in a modified corundum structure,^[35,36] and exhibits large optical rotation and intriguing chiral and polar domains.^[37] There are three Ni sites and one Te site in the formula unit. As shown in **Figure 1a**, two kinds of honeycomb layers formed by edge-sharing NiO_6 and TeO_6 octahedra stack along the c -axis, generating the polar crystal structure. Ni_IO_6 and $\text{Ni}_{\text{II}}\text{O}_6$ are ferromagnetically coupled and form one honeycomb layer, and $\text{Ni}_{\text{III}}\text{O}_6$ and TeO_6 form the other.

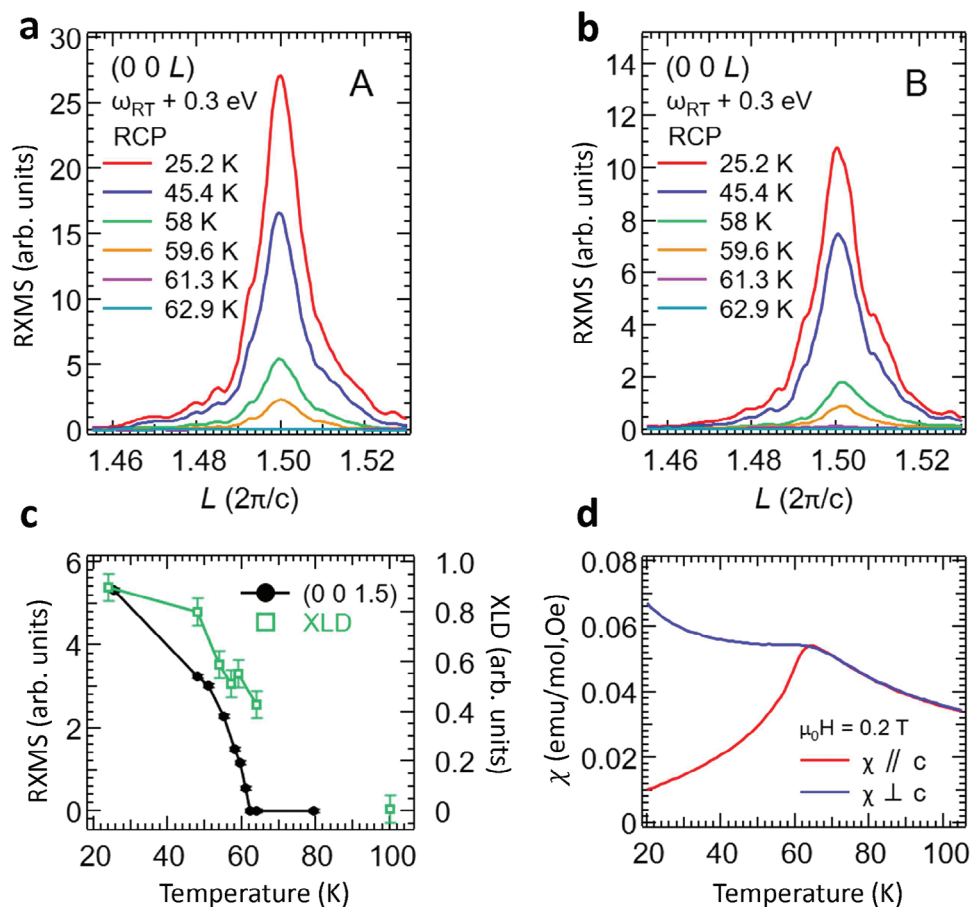


Figure 2. Magnetic transition of Ni₃TeO₆. a,b) Resonant X-ray magnetic scattering (RXMS) intensities at $\vec{q} = (00L)$ in the reciprocal space scanned along L with RCP at the photon energy of $\omega_{RT} + 0.3$ eV at various temperatures at positions A and B, respectively. Here, ω_{RT} is the Ni L_3 -edge XAS peak energy defined in Figure 3, and A and B belong to opposite chiral domains shown in Figure 4a. c) Temperature dependence of X-ray linear dichroism (XLD) and the (0, 0, 1.5) peak of RXMS at the Ni L_3 edge plotted across the Néel transition. d) DC magnetic susceptibility for magnetic field parallel and perpendicular to the c axis taken with $\mu_0 H = 0.2$ T.

Ni₁O₆ and Ni₁₁O₆ are also connected to Ni₁₁₁O₆ on one side of the honeycomb layer through corner- and face-sharing, respectively, while both are connected to Ni₁₁₁₁O₆ on the other side via corner-sharing. In addition, the relative positions of these octahedra in the ab -plane revolve along the c -axis, showing the handedness of crystal chirality,^[37] as illustrated in Figure 1b. There exist two enantiomorphic crystal structures in Ni₃TeO₆, forming the so-called Dauphiné twin, in which right-handed and left-handed chiral domains are neighboring in the crystal.^[37] Kerr rotation has been observed for each chiral domain.^[37,38] No structural phase transition has been observed from 11 to 300 K, but internal coordinates such as bond lengths and bond angles vary with temperature.^[39]

Ni₃TeO₆ undergoes a magnetic phase transition at $T_N = 52$ –62 K from a paramagnetic state to a commensurate collinear AFM state with Ising anisotropy as shown in Figure 1b.^[33,40,41] Momentum scans of resonant X-ray magnetic scattering (RXMS) at various temperatures shown in Figures 2a, b reveal that the intensity of the (0, 0, 1.5) peak appears below T_N and steadily increases with decreasing temperature, confirming that the AFM ordering occurs below T_N . Results of temperature-dependent

RXMS at the Ni L_3 edge (Figure 2a–c) and magnetic susceptibility (Figure 2d) are consistent with the collinear AFM structure of Ni₃TeO₆. The Néel temperature of the sample studied here was $T_N = 62$ K. The observed AFM transition is marked by a sharp cusp in the parallel component χ_{\parallel} of the magnetic susceptibility. These results also agree with the results of X-ray linear dichroism (XLD) shown in Figure S7 (Supporting Information) and temperature-dependent XLD plotted in Figure 2c.

2.2. Ni L -Edge XAS

The dominant electronic configuration of the Ni²⁺ ion in oxides is typically d^8 , into which the O $2p$ -to-Ni $3d$ charge-transfer configuration $d^9\bar{L}$ is hybridized as a minor ($\approx 20\%$) component.^[42] Usually, p -to- d charge-transfer is considered within a NiO₆ octahedron, but charge-transfer between neighboring NiO₆ octahedra also occurs and increases the $d^9\bar{L}$ component, if the two octahedra share corner oxygen, and the two Ni spins are aligned antiferromagnetically.^[43] This is the case for the neighboring

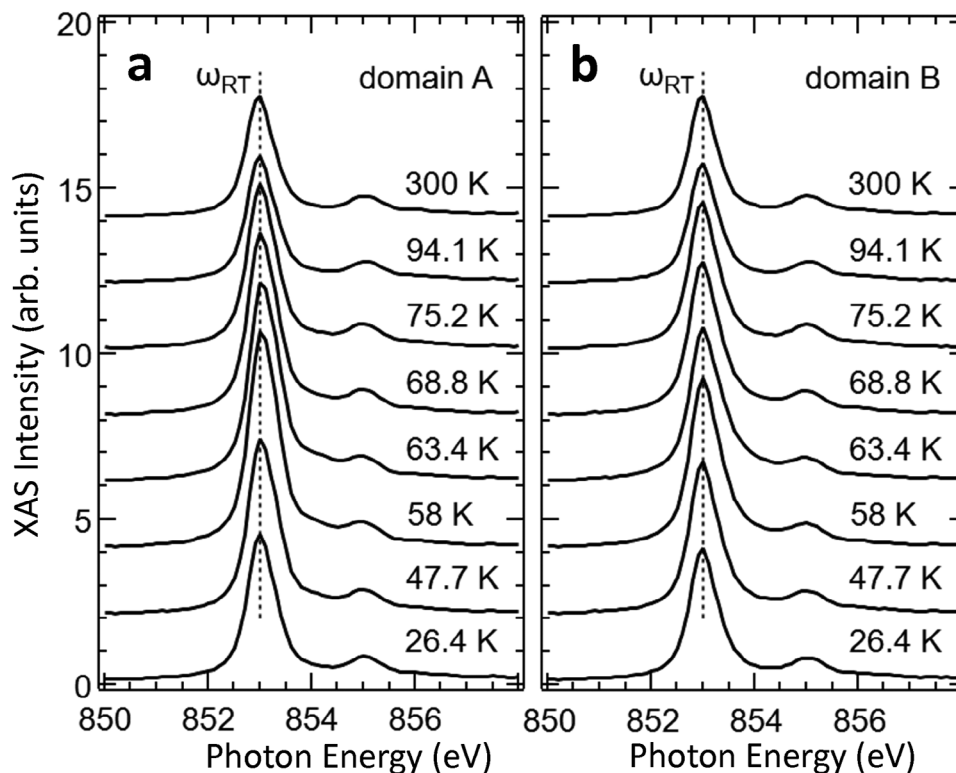


Figure 3. Temperature dependence of Ni L_3 -edge XAS of Ni_3TeO_6 . a,b) Ni L_3 -edge XAS spectra (averaged over RCP and LCP) taken at positions A and B of the sample designated in Figure 4, respectively. The incident angle θ was $\approx 53^\circ$ off the a -axis and fluorescent X-rays from the Ni_3TeO_6 sample were detected using a CCD detector. The spectra are vertically shifted for clarity. The vertical broken line shows the photon energy 853 eV ($\equiv \omega_{\text{RT}}$) of the L_3 peak at room temperature.

$\text{Ni}_I\text{O}_6/\text{Ni}_{II}\text{O}_6$ and $\text{Ni}_{III}\text{O}_6$ octahedra coupled via AFM exchange (J_4/J_3) in the collinear AFM Ni_3TeO_6 (See Figure 1b for spin structure and Figure S5, Supporting Information for exchange interactions between Ni ion).^[44]

Ni_3TeO_6 is a remarkably unique material, exhibiting both chirality and polarity. Owing to its polar $R3$ structure, polarity aligns with chirality, making it impossible to observe different polarities within the same chiral domain concurrently. We therefore studied XCD of two chiral domains by performing Ni L_3 -edge XAS measurements using circularly polarized X-rays focused on each chiral domain. Figure 3a,b plot the average of Ni L_3 -edge XAS spectra taken with RCP and LCP X-rays impinging on positions marked A and B, respectively, in a $90 \times 90\text{-}\mu\text{m}^2$ image shown in Figure 4a. This area contains two different structurally chiral domains. One can see that, around $T \approx T_N$, the peak intensity of XAS is enhanced and shifted toward higher photon energies by ≈ 0.3 eV relative to the peak position 853 eV denoted as ω_{RT} at room temperature. As explained below, this suggests an increase in the number of d holes on the Ni ions. When the temperature increases towards T_N , the AFM correlation between the neighboring ferromagnetic double layers is weakened, and the p -to- d charge transfer is reduced. This increases the weight of the d^8 configuration relative to the charge-transferred $d^9\bar{L}$ configuration and hence the number of d holes on Ni, resulting in the shift of the XAS peak toward higher photon energies and the increase of the XAS intensity simultaneously.

2.3. Emergence of Giant XCD

Surprisingly, we observed significant XCD at each domain for temperatures below $\approx T_N$, as shown in Figure 4b, despite the absence of an external magnetic field nor remanent magnetization. See the magnetization curves in Figure S3 (Supporting Information). The measured dichroic spectra, i.e., the RCP-LCP difference spectra, show a maximum magnitude of XCD about 20% of Ni L_3 -edge XAS peak, much larger than the previously reported one of 2%.^[39] and exhibit a non-linear dependence on the X-ray intensity (See Figure S4, Supporting Information plotted in Supporting Information.), showing a positive peak at $\omega_{\text{RT}} + 0.3$ eV at position A and a negative peak at $\omega_{\text{RT}} + 0.7$ eV at position B. The dichroic images shown in Figure 4c demonstrate a sign change between the domains of opposite chirality. The color contrast between the domains increases with temperature, and becomes strongest around T_N and invisibly weak at room temperature. The XCD intensities at A and B as functions of temperature plotted in Figure 4d also show a consistent tendency, particularly the enhancement below $\approx T_N$.

3. Discussion

3.1. Symmetry Analysis

Ni_3TeO_6 exhibits a chiral lattice and effective time-reversal symmetry in its ground state. The illumination of left-handed

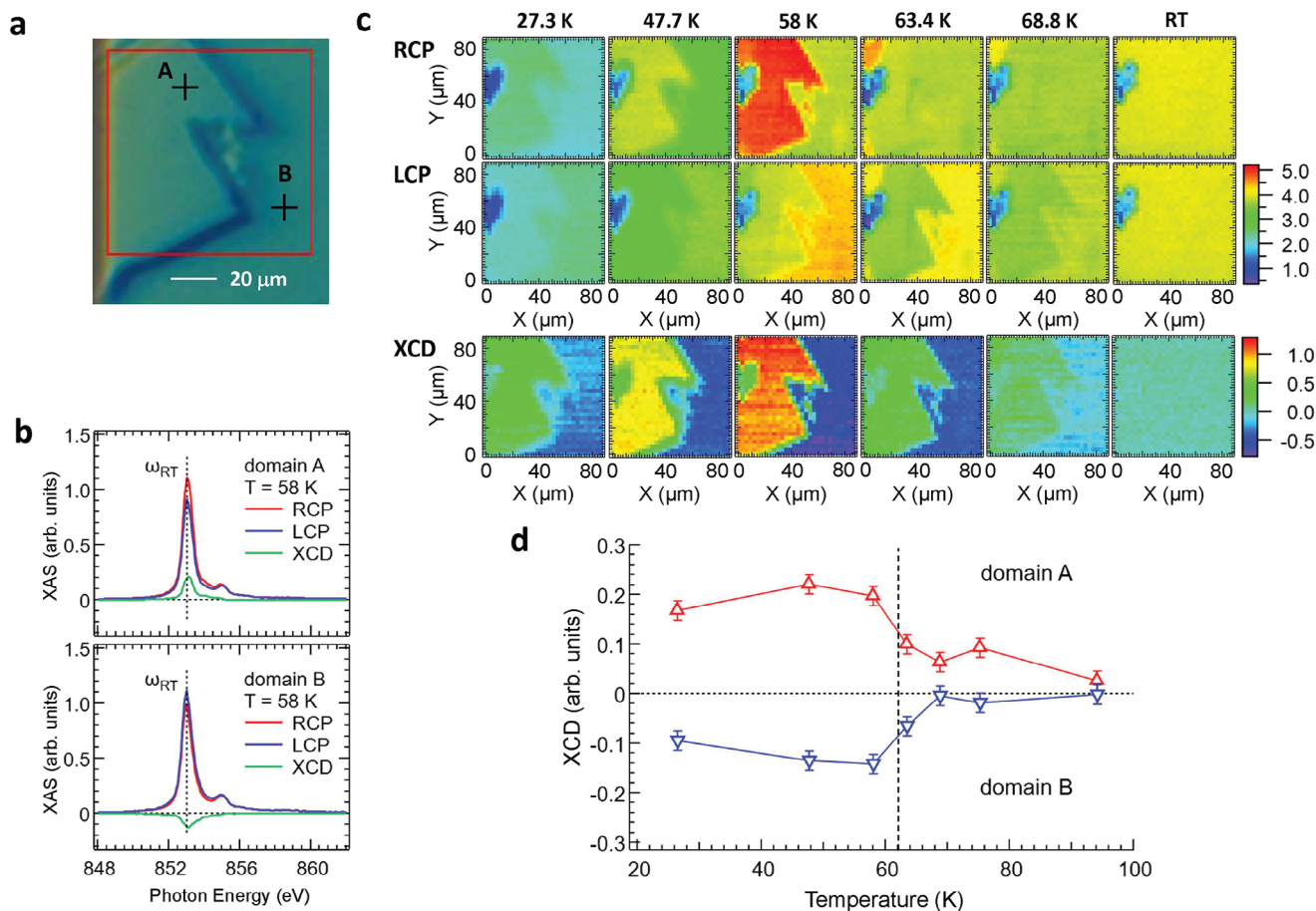


Figure 4. Temperature dependence XNCD of Ni_3TeO_6 . a) Image of the Ni_3TeO_6 sample recorded with a polarized light microscope. Horizontal and vertical edges are parallel to the $[0\ 1\ \bar{1}\ 0]$ and $[2\ \bar{1}\ \bar{1}\ 0]$ axes, respectively. The red square box shows a $90 \times 90\text{-}\mu\text{m}^2$ area on which the XAS and XCD images were taken. Positions A and B are in two different domains of opposite crystal chirality. b) XAS spectra taken at positions A and B with RCP and LCP and difference spectra, i.e., X-ray circular dichroism spectra, at 58 K measured by the fluorescence-yield method. Circular dichroism signals at A and B are positive and negative, respectively. c) XAS images of Ni_3TeO_6 in the $90 \times 90\text{-}\mu\text{m}^2$ area measured at a photon energy of $\omega_{\text{RT}} + 0.7\text{ eV}$ (photon energy of ω_{RT} at RT) with RCP (top) and LCP (middle) and RCP - LCP difference images (bottom) at various temperatures. d) XCD intensity normalized to the L_3 XAS peak intensity, defined by $2(\text{RCP} - \text{LCP})/(\text{RCP} + \text{LCP})$, at positions A and B plotted against temperature. The dichroism changes its sign between A and B.

polarized X-ray with a wave vector $+\vec{k}$ on the crystallographic left-chiral domain exhibits identical behavior to that with $-\vec{k}$. In other words, the observed XCD is reciprocal for temperatures above and below T_N . In contrast, XMCD on ferromagnets is non-reciprocal, i.e., XMCD with $+\vec{k}$ is different from that with $-\vec{k}$. In an AFM state, XMCD signals are typically canceled between the opposite magnetic moments, and only weak XMCD signals can be observed under a strong external magnetic field through the field-induced uniform magnetization (typically of $\approx 0.1\ \mu_B$ per Ni atom under a field of $\approx 1\text{ T}$). The magnitude of the observed XCD in Ni_3TeO_6 is comparable to the XMCD of $3d$ transition metals but much larger than the usual XNCD resulting from the E1-E2 interference. This phenomenon is a new type of XCD with a mechanism beyond the E1-E2 interference. The XCD observed in the present study appears to be comparable with the XMCD of a magnetic moment of order μ_B per Ni atom despite the absence of an external magnetic field. Since there are equal numbers of spin-up and spin-down Ni atoms in the

collinear AFM state, the XCD signals arising from spin moments must be canceled unless there were a uniform “effective magnetic field” that has not been considered in conventional XMCD mechanisms.

A possible origin of the “effective magnetic field” is the crystal chirality of each domain (Figure 1b) because the chirality is uniform in each domain and the dichroic signal changes its sign between the domains. The crystal chirality alone does not break “effective” \mathcal{T} symmetry and can lead only to tiny XNCD signals. It, therefore, cannot explain the appreciable dichroic intensity enhancement below T_N as remarked above. From the viewpoint of symmetry, the total Hamiltonian of the whole system including Ni_3TeO_6 and X-rays should be invariant under the simultaneous transformations of charge conjugation, parity (\mathcal{P}), and \mathcal{T} .^[45] For temperatures above T_N , the coupling of circularly polarized X-rays to crystal chirality makes the photon-matter interaction symmetric under \mathcal{P} transformation (more precisely, mirror-image transformation). That is, an observation of XNCD requires that the sample has a broken \mathcal{PT} symmetry.

3.2. Origin of the X-Ray Circular Dichroism

The enhancement of XCD in Ni_3TeO_6 below T_N must arise from the coupling of X-rays to the magnetic order in the presence of crystal chirality. We propose a theory that is consistent with the symmetry analysis^[34] to understand this intriguing giant XNCD. Theoretically, to the linear order, the EM fields of X-ray generally induce the coupling of electric current \vec{j} to the vector potential \vec{A} as $-\int d^3\vec{r} \vec{j} \cdot \vec{A}$. As shown in the Supporting Information, the transverse part of the current operator can be written as the magnetization current due to the orbital magnetization, and the EM fields of X-ray induces a coupling as $-\int d^3\vec{r} \vec{B} \cdot \vec{M}$. In other words, the movement of X-ray photons within a chiral crystal behaves as a magnetic field. The chiral structure of Ni_3TeO_6 ensures a non-zero average orbital magnetization. In turn, orbital magnetization will be induced, and through spin-orbit coupling (SOC), spin polarization is further generated. When the wave vector of X-rays is changed from $+\vec{k}$ to $-\vec{k}$, the Poynting vector $\vec{E} \times \vec{B}$ is also reversed and this can be viewed as \vec{B} goes to $-\vec{B}$. Hence, the induced orbital magnetization also changes sign. If \vec{k} is parallel to the axis of a chiral structure that only breaks the mirror symmetry, the orbital current in the chiral structure is reversed with the same magnitude. The reversed orbital magnetization thus has same magnitude so that the net effect is that \vec{M} goes to $-\vec{M}$. The observed XCD thus is reciprocal, and the reciprocity justifies its name as an XNCD, rather than XMCD.

Microscopically, the Berry curvature^[46–48] can be also regarded as an effective magnetic field in k space; it will create circular motion of electrons, resulting in the orbital moment, which can be probed by dipole transition using circular polarized light. The induced orbital magnetization in the momentum space is reflected as the splitting of the quasi-particle energies and is proportional to the Berry curvature.^[47] The Berry curvature vanishes for systems possessing both inversion symmetry and time reversal symmetry. In the case of a system with time reversal symmetry but lacking inversion symmetry, nonvanishing Berry curvature exists. Formally, we have proved that the XCD cross section of L -edge XAS is proportional to the integration of Berry curvature over momentum at a fixed energy (refer to Equation (S37), Supporting Information). In accordance with the XMCD sum rule,^[11] the energy integration of XCD is proportional to the integration of Berry curvature across the entire momentum space, leading to an orbital moment.^[47] The connection of XCD to the Berry curvature is important in shaping our understanding of the magnetic properties of materials because we do not necessarily need time-reversal symmetry broken to obtain XCD. Indeed, the non-vanishing Berry curvature in Ni_3TeO_6 results from inversion-symmetry broken, forming a class of materials different from those based on time-reversal symmetry broken.

Our model agrees with the observation of current-induced magnetization in a chiral semiconductor Te, where SOC is strong.^[49,50] The incident X-rays can induce chiral phonons and magnons in Ni_3TeO_6 as it exhibits a chiral structure and SOC is also strong due to the presence of the Te atoms. The angular momenta of the X-rays eventually develop through the creation of such phonons and magnons and continue to enhance the XNCD. In CISS, an electric current injected through chi-

ral molecules^[32,51] or crystals,^[30] the chiral structure induces spin polarization in a preferred direction and imparts significant spin selectivity to the charge current. Similar spin selectivity has also been observed for chiral molecules even without a charge current.^[52] In the insulating Ni_3TeO_6 , a finite heat current due to nonequilibrium phonons and magnons can develop along the temperature gradient^[53] and flow instead of a charge current, creating a phonon angular momentum.^[54] The spin polarization induced by the incident X-ray in the chiral structure is subsequently enhanced by this “thermal CISS” effect through the excitation of relevant phonons and magnons.

The existence of giant XNCD in Ni_3TeO_6 is related to its altermagnetism—magnetic states with AFM spins in which the symmetry allows for typical ferromagnetic behaviors. The observed XNCD shows a strong temperature dependency like the XMCD from a ferromagnet across its magnetic phase transition, revealing the characteristic of altermagnetism. Ni_3TeO_6 has a symmetry corresponding to the magnetic point group of $31'$ and is categorized as a type-III altermagnet,^[26] that has broken \mathcal{PT} symmetry and does not exhibit odd-order anomalous Hall effect. A type-III altermagnet exhibits ferromagnetic behaviors only with external perturbations that conserve \mathcal{PT} symmetry. In the present XNCD measurement, the significant enhancement in the XNCD of Ni_3TeO_6 across T_N reveals its altermagnetism; the moving X-ray photons serve as the external perturbations, and induce magnetization along the X-ray moving direction.

Additionally, the observed giant XNCD appears to reflect the magnetic susceptibility of Ni_3TeO_6 . The observation XNCD below T_N with a magnitude comparable to that of XMCD suggests an effective coupling between spin and chirality. Although the orbital magnetization is time-reversal odd and it alone can't couple to the structural chirality directly, the combination of X-ray propagation and its induced magnetization is time-reversal even, like structural chirality. RXMS intensity maps depicted in Figure S2 (Supporting Information) show images consistent with chiral structure images, supporting the above scheme of effective spin-chiral coupling. Therefore, the propagation of incident X-rays in a chiral structure generates an effective magnetic field capable of inducing an orbital magnetic moment and hence spin polarization through SOC. Consequently, the XNCD measurement contains the magnetic susceptibility χ . Temperature-dependent XNCD results, as shown in Figure 4d, demonstrate a finite magnetic susceptibility in Ni_3TeO_6 above T_N . The increase in XNCD near T_N corresponds to the rise in χ as depicted in Figure 2d. Below T_N , XNCD encompasses both χ_{\perp} and χ_{\parallel} for the AFM state and the contribution from the AFM order itself, resulting in the cusp-like feature of the AFM state. The direction and magnitude of the spin polarization would be determined by a balance between the incident direction of the X-rays, which favors the c direction, and the magnetic anisotropy of Ni_3TeO_6 , which favors the ab direction. This may be the origin of the incident angle dependence of the XCD intensity that is maximized around $\theta \approx 53^\circ$. (See Figure S8, Supporting Information)

4. Conclusion

In conclusion, we have studied XCD at the Ni $L_{2,3}$ edge of the structurally chiral, collinear antiferromagnet Ni_3TeO_6 , and observed strong XNCD signals without an external magnetic

field. Distinct from XMCD in noncoplanar antiferromagnets, this XNCD is significantly enhanced by AFM order and changes sign between domains of opposite crystal chirality. The mechanism of the magnetic enhancement of XNCD is beyond the conventional understanding that most collinear antiferromagnets should exhibit no XMCD because of \mathcal{T} symmetry. To explain this new type of XNCD, we propose a model based on symmetry analysis, in analogy to current-induced magnetization in chiral lattice. Our observations provide compelling evidence that supports a novel understanding of the mechanism of XNCD in a chiral material. Our results show that it does not necessarily need to break (effective) time-reversal symmetry to have circular dichroism in magnetic materials. The new mechanism is through the non-vanishing Berry curvature due to the inversion-symmetry broken. This is distinctly different from all previous examples of AF materials that exhibit circular dichroism due to broken time-reversal symmetry. Our results reveal the altermagnetism of Ni_3TeO_6 and establish the first example of a new class of magnetic materials that can exhibit circular dichroism with time-reversal symmetry. Furthermore, our method can be used as a new spectroscopic tool to study magnetic materials, especially those relevant to chiral spintronics.

5. Experimental Section

Ni *L*-edge soft X-ray spectroscopy and scattering measurements were conducted at Beamline 41A of the Taiwan Photon Source.^[55] Figure S1 (Supporting Information) depicts the experimental geometry of the soft-X-ray measurements. The Ni_3TeO_6 single crystals used in this study were grown via a flux method; detailed growth conditions were available in Reference.^[40] DC magnetic susceptibility measurements, using a magnetic field of $\mu_0 H = 0.2$ T parallel and perpendicular to the *c*-axis, show the typical temperature dependence expected for a collinear antiferromagnet with the spin direction aligned parallel to the *c*-axis.

For RXMS, XAS, and circular dichroism measurements, incident X-rays were employed with an energy resolution of 0.3 eV, focused to a lateral size of approximately $1\ \mu\text{m}$ at the sample position using a capillary tube optic. The scattered X-rays and fluorescence emitted from the Ni_3TeO_6 sample to the direction perpendicular to the incident X-rays were detected using a photodiode and a CCD detector. Total-fluorescence-yield (TFY) measurements with self-absorption correction^[56] were conducted for XAS and circular dichroism. XLD measurements involved with soft X-rays of $50\ \mu\text{m}$ in vertical and $60\ \mu\text{m}$ in horizontal, incident on the sample with $\theta = 20^\circ$ off the *a*-axis, were obtained via the partial-fluorescence-yield (PFY) method. Additional details can be found in the Supporting Information.

Statistical Analysis: XAS spectral intensities, initially normalized to the incident X-ray flux and after background subtraction, underwent further normalization at 8 eV (5 eV) below the L_3 edge and 8 eV (5 eV) above the L_2 edge for TFY-XAS (PFY-XAS). RXMS scans were normalized to the average incident X-ray intensity measured by the photodiode before and after the scans. All statistical analyses pertaining to RXMS and XAS intensities were conducted by using Igor Pro software with data errors of $\pm 1\%$ of the maximum intensity and $\pm 2\%$ of the L_3 -edge XAS peak intensity for XCD.

Supporting Information

Supporting Information is available from the Wiley Online Library or from the author.

Acknowledgements

The authors acknowledged the contributions of T. A. W. Beale, W. B. Wu, P. D. Hatton, and T. Tyliczszak to the construction of the soft X-ray diffrac-

tometer TACoDE. The authors thank Yusuke Kato and Jun-ichiro Kishine for discussion on CISS effects, and Wei-En Ke for help with magnetization measurements. This work was partly supported by the National Science and Technology Council of Taiwan under Grant no. 109-2112-M-213-010-MY3 and 110-2923-M-213-001 and by the Japan Society for the Promotion of Science under Grant no. JP22K03535. The work at Rutgers was supported by W. M. Keck Foundation. A.F. acknowledged the support from the Yushan Fellow Program under the Ministry of Education of Taiwan.

Conflict of Interest

The authors declare no conflict of interest.

Data Availability Statement

The data that support the findings of this study are available in the supplementary material of this article.

Keywords

chiral crystal, collinear altermagnet, X-ray circular dichroism

Received: September 6, 2023

Revised: February 9, 2024

Published online: April 10, 2024

- [1] L. Alagna, T. Proserpi, S. Turchini, J. Goulon, A. Rogalev, C. Goulon-Ginet, C. R. Natoli, R. D. Peacock, B. Stewart, *Phys. Rev. Lett.* **1998**, *80*, 4799.
- [2] J. Goulon, C. Goulon-Ginet, A. Rogalev, V. Gotte, C. Malgrange, C. Brouder, C. R. Natoli, *J. Chem. Phys.* **1998**, *108*, 6394.
- [3] A. P. Oreshko, E. N. Ovchinnikova, A. Rogalev, F. Wilhelm, B. V. Mill, V. E. Dmitrienko, *J. Synchrotron Radiat.* **2018**, *25*, 222.
- [4] J. Goulon, A. Rogalev, F. Wilhelm, N. Jaouen, C. Goulon-Ginet, C. Brouder, *J. Phys.: Condens. Matter* **2003**, *15*, S633.
- [5] D. J. Huang, C. F. Chang, H.-T. Jeng, G. Guo, H.-J. Lin, W. Wu, H. Ku, A. Fujimori, Y. Takahashi, C. T. Chen, *Phys. Rev. Lett.* **2004**, *93*, 077204.
- [6] T. Kurumaji, S. Ishiwata, Y. Tokura, *Phys. Rev. X* **2015**, *5*, 031034.
- [7] H. S. Bennett, E. A. Stern, *Phys. Rev.* **1965**, *137*, A448.
- [8] J. L. Erskine, E. A. Stern, *Phys. Rev. B* **1975**, *12*, 5016.
- [9] G. Schütz, W. Wagner, W. Wilhelm, P. Kienle, R. Zeller, R. Frahm, G. Materlik, *Phys. Rev. Lett.* **1987**, *58*, 737.
- [10] C. T. Chen, F. Sette, Y. Ma, S. Modesti, *Phys. Rev. B* **1990**, *42*, 7262.
- [11] B. T. Thole, P. Carra, F. Sette, G. van der Laan, *Phys. Rev. Lett.* **1992**, *68*, 1943.
- [12] P. Carra, B. T. Thole, M. Altarelli, X. Wang, *Phys. Rev. Lett.* **1993**, *70*, 694.
- [13] J. Stöhr, H. Padmore, S. Anders, T. Stammler, M. Scheinfein, *Surf. Rev. Lett.* **1998**, *5*, 1297.
- [14] A. Rogalev, F. Wilhelm, N. Jaouen, J. Goulon, J.-P. Kappler, in *Magnetism: a synchrotron radiation approach*, Springer, Berlin, Heidelberg **2006**, pp. 71–93.
- [15] W. Feng, J.-P. Hanke, X. Zhou, G.-Y. Guo, S. Blügel, Y. Mokrousov, Y. Yao, *Nat. Commun.* **2020**, *11*, 118.
- [16] Y. Yamasaki, H. Nakao, T.-h. Arima, *J. Phys. Soc. Jpn.* **2020**, *89*, 083703.
- [17] N. Sasabe, M. Kimata, T. Nakamura, *Phys. Rev. Lett.* **2021**, *126*, 157402.
- [18] G. van der Laan, *Phys. Rev. B* **2021**, *104*, 094414.
- [19] S. Wimmer, S. Mankovsky, H. Ebert, *Phys. Rev. B* **2021**, *103*, 024437.

- [20] M. Kimata, N. Sasabe, K. Kurita, Y. Yamasaki, C. Tabata, Y. Yokoyama, Y. Kotani, M. Ikhlas, T. Tomita, K. Amemiya, H. Nojiri, S. Nakatsuji, T. Koretsune, H. Nakao, T.-h. Arima, T. Nakamura, *Nat. Commun.* **2021**, 12, 5582.
- [21] S. Sakamoto, T. Higo, M. Shiga, K. Amemiya, S. Nakatsuji, S. Miwa, *Phys. Rev. B* **2021**, 104, 134431.
- [22] S.-W. Cheong, *npj Quantum Mater.* **2020**, 5, 37.
- [23] L. Šmejkal, J. Sinova, T. Jungwirth, *Phys. Rev. X* **2022**, 12, 031042.
- [24] L. Šmejkal, J. Sinova, T. Jungwirth, *Phys. Rev. X* **2022**, 12, 040501.
- [25] I. Mazin, *Phys. Rev. X* **2022**, 12, 040002.
- [26] S.-W. Cheong, F.-T. Huang, *npj Quantum Mater.* **2024**, 9, 13.
- [27] A. Hariki, A. Dal Din, O. J. Amin, T. Yamaguchi, A. Badura, D. Kriegner, K. W. Edmonds, R. P. Champion, P. Wadley, D. Backes, L. S. I. Weiga, S. S. Dhesi, G. Springholz, L. Šmejkal, K. Výborný, T. Jungwirth, J. Kunes, *arXiv:2305.03588* **2023**.
- [28] R. D. Peacock, B. Stewart, *J. Phys. Chem. B* **2001**, 105, 351.
- [29] L. Šmejkal, R. González-Hernández, T. Jungwirth, J. Sinova, *Sci. Adv.* **2020**, 6, eaaz8809.
- [30] A. Inui, R. Aoki, Y. Nishiue, K. Shiota, Y. Kousaka, H. Shishido, D. Hirobe, M. Suda, J.-i. Ohe, J.-i. Kishine, H. M. Yamamoto, Y. Togawa, *Phys. Rev. Lett.* **2020**, 124, 166602.
- [31] B. Göhler, V. Hamelbeck, T. Z. Markus, M. Kettner, G. F. Hanne, Z. Vager, R. Naaman, H. Zacharias, *Science* **2011**, 331, 894.
- [32] R. Naaman, D. H. Waldeck, *J. Phys. Chem. Lett.* **2012**, 3, 2178.
- [33] I. Živković, K. Prša, O. Zaharko, H. Berger, *J. Phys. Condens. Matter* **2010**, 22, 056002.
- [34] S.-W. Cheong, *npj Quantum Mater.* **2019**, 4, 53.
- [35] R. Newnham, E. Meagher, *Mater. Res. Bull.* **1967**, 2, 549.
- [36] R. Becker, H. Berger, *Acta Crystallogr. E* **2006**, 62, i222.
- [37] X. Wang, F.-T. Huang, J. Yang, Y. S. Oh, S.-W. Cheong, *APL Mater.* **2015**, 3, 076105.
- [38] M. Langenbach, *Dissertation (Universität zu Köln, 2019)* **2019**.
- [39] A. Ghosh, K.-H. Chen, X.-S. Qiu, S.-H. Hsieh, Y.-C. Shao, C.-H. Du, H.-T. Wang, Y.-Y. Chin, J.-W. Chiou, S. C. Ray, H.-M. Tsai, C.-W. Pao, H.-J. Lin, J.-F. Lee, R. Sankar, F.-C. Chou, W.-F. Pong, *Sci. Rep.* **2018**, 8, 15779.
- [40] Y. S. Oh, S. Artyukhin, J. J. Yang, V. Zapf, J. W. Kim, D. Vanderbilt, S.-W. Cheong, *Nat. Commun.* **2014**, 5, 3201.
- [41] J. W. Kim, S. Artyukhin, E. D. Mun, M. Jaime, N. Harrison, A. Hansen, J. J. Yang, Y. S. Oh, D. Vanderbilt, V. S. Zapf, S.-W. Cheong, *Phys. Rev. Lett.* **2015**, 115, 137201.
- [42] A. Fujimori, F. Minami, *Phys. Rev. B* **1984**, 30, 957.
- [43] M. A. van Veenendaal, G. A. Sawatzky, *Phys. Rev. Lett.* **1993**, 70, 2459.
- [44] F. Wu, E. Kan, C. Tian, M.-H. Whangbo, *Inorg. Chem.* **2010**, 49, 7545.
- [45] A. S. Blum, A. Martínez de Velasco, *Eur. Phys. J. H* **2022**, 47, 5.
- [46] M. V. Berry, *Proc. R. Soc. London. A. Math. Phys. Sci.* **1984**, 392, 45.
- [47] D. Xiao, J. Shi, Q. Niu, *Phys. Rev. Lett.* **2005**, 95, 137204.
- [48] D. Xiao, M.-C. Chang, Q. Niu, *Rev. Mod. Phys.* **2010**, 82, 1959.
- [49] L. E. Vorob'ev, E. L. Ivchenko, G. E. Pikus, I. I. Farbshtein, V. A. Shalygin, A. V. Shturbin, *JETP Lett.* **1979**, 29, 441.
- [50] T. Furukawa, Y. Shimokawa, K. Kobayashi, T. Itou, *Nat. Commun.* **2017**, 8, 954.
- [51] K. Ray, S. P. Ananthavel, D. H. Waldeck, R. Naaman, *Science* **1999**, 283, 814.
- [52] K. Kondou, M. Shiga, S. Sakamoto, H. Inuzuka, A. Nihonyanagi, F. Araoka, M. Kobayashi, S. Miwa, D. Miyajima, Y. Otani, *J. Am. Chem. Soc.* **2022**, 144, 7302.
- [53] H. Yang, X. Xu, J. H. Lee, Y. S. Oh, S.-W. Cheong, J.-G. Park, *Phys. Rev. B* **2022**, 106, 144417.
- [54] M. Hamada, E. Minamitani, M. Hirayama, S. Murakami, *Phys. Rev. Lett.* **2018**, 121, 175301.
- [55] A. Singh, H. Y. Huang, Y. Y. Chu, C. Y. Hua, S. W. Lin, H. S. Fung, H. W. Shiu, J. Chang, J. H. Li, J. Okamoto, C. C. Chiu, C. H. Chang, W. B. Wu, S. Y. Perng, S. C. Chung, K. Y. Kao, S. C. Yeh, H. Y. Chao, J. H. Chen, D. J. Huang, C. T. Chen, *J. Synchrotron Radiat.* **2021**, 28, 977.
- [56] S. S. Eisebitt, T. Böske, J.-E. Rubensson, W. Eberhardt, *Phys. Rev. B* **1993**, 47, 14103.